

Article

Preparation of Hollow Core–Shell Fe₃O₄/Nitrogen-Doped Carbon Nanocomposites for Lithium-Ion Batteries

Jie Wang¹, Qin Hu^{1,2}, Wenhui Hu¹, Wei Zhu¹, Ying Wei¹, Kunming Pan^{3,*}, Mingbo Zheng^{1,4,*} and Huan Pang^{1,*}

¹ School of Chemistry and Chemical Engineering, Yangzhou University, Yangzhou 225002, China; wj1159785@163.com (J.W.); huqinchemistry@foxmail.com (Q.H.); huwenhui0919@163.com (W.H.); zhuwei_77@163.com (W.Z.); 13206588726@163.com (Y.W.)

² Hengshanqiao Senior Middle School, Wujin District, Changzhou 213119, China

³ National Joint Engineering Research Center for Abrasion Control and Molding of Metal Materials & Henan Key Laboratory of High-Temperature Structural and Functional Materials, Henan University of Science and Technology, Luoyang 471003, China

⁴ College of Materials Science and Technology, Nanjing University of Aeronautics and Astronautics, Nanjing 210016, China

* Correspondence: pankunming2008@haust.edu.cn (K.P.); zhengmingbo@nuaa.edu.cn (M.Z.); huanpangchem@hotmail.com (H.P.)

Abstract: Iron oxides are potential electrode materials for lithium-ion batteries because of their high theoretical capacities, low cost, rich resources, and their non-polluting properties. However, iron oxides demonstrate large volume expansion during the lithium intercalation process, resulting in the electrode material being crushed, which always results in poor cycle performance. In this paper, to solve the above problem, iron oxide/carbon nanocomposites with a hollow core–shell structure were designed. Firstly, an Fe₂O₃@polydopamine nanocomposite was prepared using an Fe₂O₃ nanocube and dopamine hydrochloride as precursors. Secondly, an Fe₃O₄@N-doped C composite was obtained by means of further carbonization treatment. Finally, Fe₃O₄@void@N-Doped C-*x* composites with core–shell structures with different void sizes were obtained by means of Fe₃O₄ etching. The effect of the etching time on the void size was studied. The electrochemical properties of the composites when used as lithium-ion battery materials were studied in more detail. The results showed that the sample that was obtained via etching for 5 h using 2 mol L^{−1} HCl solution at 30 °C demonstrated better electrochemical performance. The discharge capacity of the Fe₃O₄@void@N-Doped C-5 was able to reach up to 1222 mA g h^{−1} under 200 mA g^{−1} after 100 cycles.

Keywords: hollow core–shell structure; iron oxide; lithium-ion batteries



Citation: Wang, J.; Hu, Q.; Hu, W.; Zhu, W.; Wei, Y.; Pan, K.; Zheng, M.; Pang, H. Preparation of Hollow Core–Shell Fe₃O₄/Nitrogen-Doped Carbon Nanocomposites for Lithium-Ion Batteries. *Molecules* **2022**, *27*, 396. <https://doi.org/10.3390/molecules27020396>

Academic Editor: Tao Wang

Received: 30 November 2021

Accepted: 5 January 2022

Published: 8 January 2022

Publisher's Note: MDPI stays neutral with regard to jurisdictional claims in published maps and institutional affiliations.



Copyright: © 2022 by the authors. Licensee MDPI, Basel, Switzerland. This article is an open access article distributed under the terms and conditions of the Creative Commons Attribution (CC BY) license (<https://creativecommons.org/licenses/by/4.0/>).

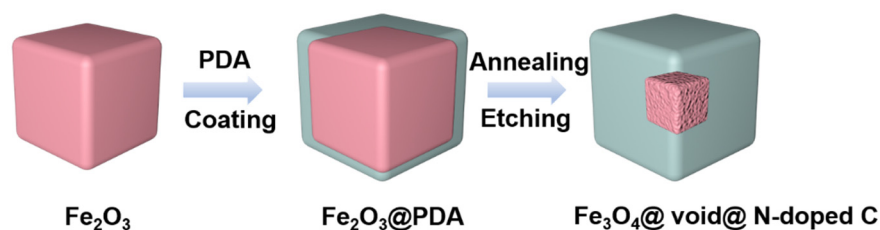
1. Introduction

With the rapid development of the global economy, the shortage of fossil fuels and the worsening of environmental pollution have become a great threat to mankind. Therefore, people must develop green and environmentally friendly clean energy to replace traditional fossil fuels [1–4]. Solar, wind, and tidal energy are renewable and result in lower levels of pollution, making electricity generated from them a good alternative [5–8]. However, these sources are often intermittently limited. Electrochemical energy storage provides a feasible way to store electric energy [9–12]. On the one hand, it can solve the intermittence problem of the above energy sources. On the other hand, this allows the mobile storage of energy. Among various electrochemical energy storage devices, lithium-ion batteries have attracted more and more attention because of their high energy density, long life cycle, and environmental friendliness [13–17].

As an important branch of anode materials for lithium-ion batteries, transition metal oxides (M_xO_y, M = Fe, Co, Ni, Cu, Mn, etc.) have attracted more and more attention. The

conversion reaction between transition metal oxides and lithium ion means that they have a high lithium storage capacity [18–22]: $M_xO_y + 2yLi^+ + 2ye^- = yLi_2O + xM$. In general, transition metal oxides have a significantly higher theoretical specific capacity than graphite when used as anode materials for lithium-ion batteries [23–25]. However, it is inevitable that transition metal oxides will experience large volume deformation during the cycling process, which leads to the pulverization of the electrode materials and also results in serious capacity fading [26–29]. Researchers have started to pay a great deal of attention to one of the transition metal oxides, iron oxide (FeO_x). Compared to other metal oxides, such as CoO_x and NiO , FeO_x has the advantages of being a cheap and abundant resource that is also environmentally friendly [30–32]. However, the volume expansion effect and low electrical conductivity limit the application of FeO_x in production [30,33–35].

Forming composite materials with a carbon coating is an effective way to improve the performance of iron oxides [36,37]. On the one hand, carbon coating can improve the electrical conductivity of electrode materials. On the other hand, it can alleviate the volume expansion effect of iron oxides during the cycling process [36,37]. The conductivity of carbon materials obtained via the carbonization of common carbon sources is usually not good. By doping carbon with nitrogen, the conductivity of carbon materials can be greatly improved in order to better improve the electrochemical performance of iron oxides [38–46]. In addition, relevant studies show that the nano-cavity structure can accommodate the volume deformation of the electrode material well during the cycling process, thus improving the cycling performance of the material [47,48]. In this work, Fe_2O_3 cubes with uniform size are prepared by means of the hydrothermal method. Then, polydopamine is coated on the surface of Fe_2O_3 cubes. After carbonization, Fe_3O_4 @nitrogen-doped carbon (N-doped C) composites are formed (Scheme 1). The composite is further etched with hydrochloric acid to prepare the core-shell Fe_3O_4 @void@N-doped C nanocomposites (Scheme 1). The void size of the nanocomposites can be regulated via controlling the etching time, improving the performance of FeO_x so that it can be used as the electrode material in lithium-ion batteries. A series of Fe_3O_4 @void@N-doped C-*x* nanocomposites (*x* is 2, 5, and 10, representing the etching time of 2 h, 5 h and 10 h, respectively) were obtained by etching the carbonized product in acid different numbers of times.



Scheme 1. Schematic illustration of the fabrication of Fe_3O_4 @void@N-doped C.

2. Results and Discussion

Figure S1a (see Supplementary Materials) shows the X-ray diffraction (XRD) pattern of the Fe_2O_3 precursor. Compared to the standard cards, the characteristic peaks of the Fe_2O_3 cube samples are consistent with the standard peaks of α - Fe_2O_3 (JCPDS:33-0664). Figure S1b shows the XRD pattern of an Fe_3O_4 @void@N-doped C-2 composite. Compared to the standard card (JCPDS:19-0629), it can be seen that the main characteristic peaks of Fe_3O_4 @void@N-doped C-2 are consistent with the standard peaks of Fe_3O_4 , and the impurity peaks of FeO also appear. This shows that during the carbonization process, most of the Fe_2O_3 is converted into Fe_3O_4 and that some of it is converted into FeO.

Figure 1a,b and Figure S2a are scanning electron microscope (SEM) and transmission electron microscope (TEM) images of an Fe_2O_3 precursor. A large area of cubes with an average size of about 600 nm can be clearly observed. Figures 1c and S3a,b are SEM images of an Fe_2O_3 @PDA composite material. It can be observed that the Fe_2O_3 cube is coated with a dopamine nanolayer. Figure 1d is a TEM image of the Fe_2O_3 @PDA cube. It is more obvious that the Fe_2O_3 cube is coated with a dopamine nanolayer, and the average

thickness of the coated PDA layer is about 25 nm. Figures 1e,f and S4a,b are SEM and TEM images of the heat-treated $\text{Fe}_3\text{O}_4@\text{N-doped C}$ sample. It can also be clearly observed from Figure 1e and Figure S5a,b that voids appear in each cube. This is because the Fe_2O_3 cube is converted into Fe_3O_4 and FeO under the reductive atmosphere that is generated by dopamine in the process of high temperature carbonization, resulting in volume shrinkage. From the TEM image in Figure 1f, the carbon layer structure and hollow groove structure on the surface of the cube can be observed more clearly.

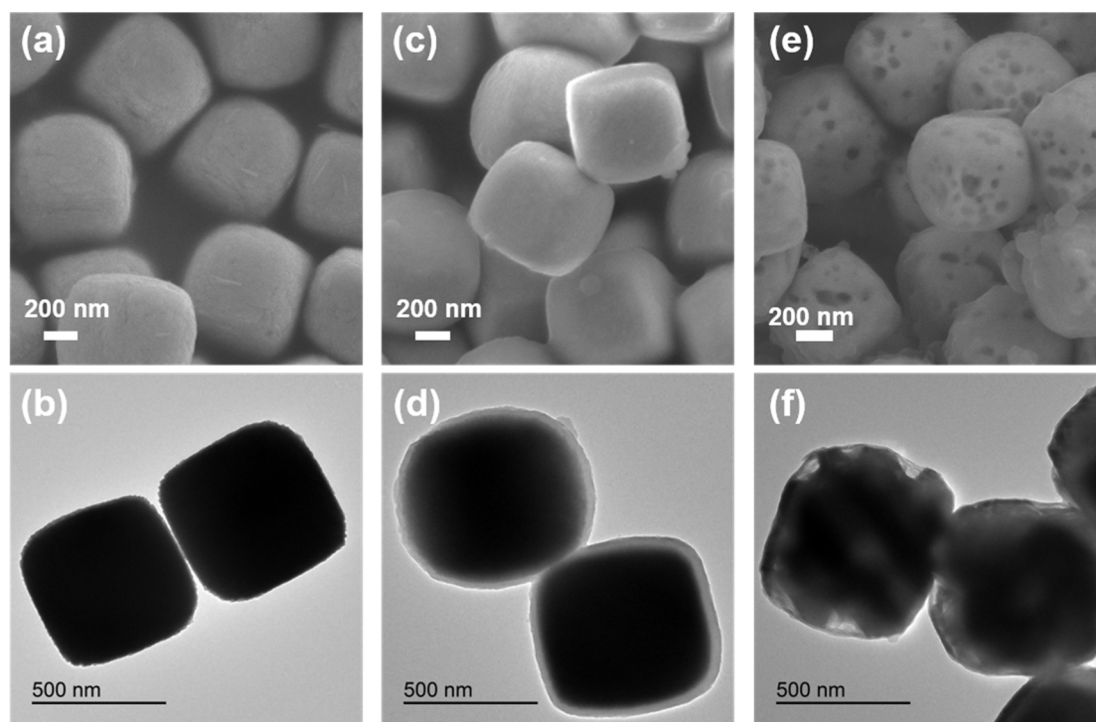


Figure 1. (a,b) SEM and TEM images of Fe_2O_3 precursor; (c,d) SEM and TEM images of cube $\text{Fe}_2\text{O}_3@\text{PDA}$; (e,f) SEM and TEM images of $\text{Fe}_3\text{O}_4@\text{N-doped C}$ sample.

Figure 2a,b are the SEM and TEM images of $\text{Fe}_3\text{O}_4@\text{void}@\text{N-doped C-2}$. It can be seen that the void in the cube is obviously larger than the carbonization product before treatment. After 5 h of etching under the same conditions, it can be observed that the void in the cube becomes larger, that some Fe_3O_4 particles present a hollow structure, and that the core-shell structure is more obvious (Figure 2c,d). After 10 h of etching, it can be observed from Figure 2e,f that the void in the cube continued to grow. This shows that the longer the etching time in hydrochloric acid is at a certain concentration, the larger the corresponding void will be. In addition, Figure 2g,h show that the internal Fe_3O_4 of the $\text{Fe}_3\text{O}_4@\text{N-doped C}$ composite has been completely etched after 2 h of etching with 4 mol L^{-1} hydrochloric acid at $30 \text{ }^\circ\text{C}$, forming a hollow carbon cube structure. The above results show that the overall morphology of the material basically does not change before and after heat treatment, and the external carbon layer can still cover the Fe_3O_4 particle. After a certain etching period, the core-shell structure is formed. Thermogravimetric analysis (TG) was used to detect the carbon content of the composites (Figure S5). It can be seen from the test results that the mass increases from about $225 \text{ }^\circ\text{C}$. This is because Fe_3O_4 is gradually oxidized into Fe_2O_3 as the temperature increases. The apparent subsequent weightlessness corresponds to the oxidation of carbon to CO_2 . After the calculation, the carbon contents of the $\text{Fe}_3\text{O}_4@\text{void}@\text{N-doped C-x}$ composites ($x = 2, 5$ and 10) were determined to be 6.3%, 11.7%, and 20.0%, respectively.

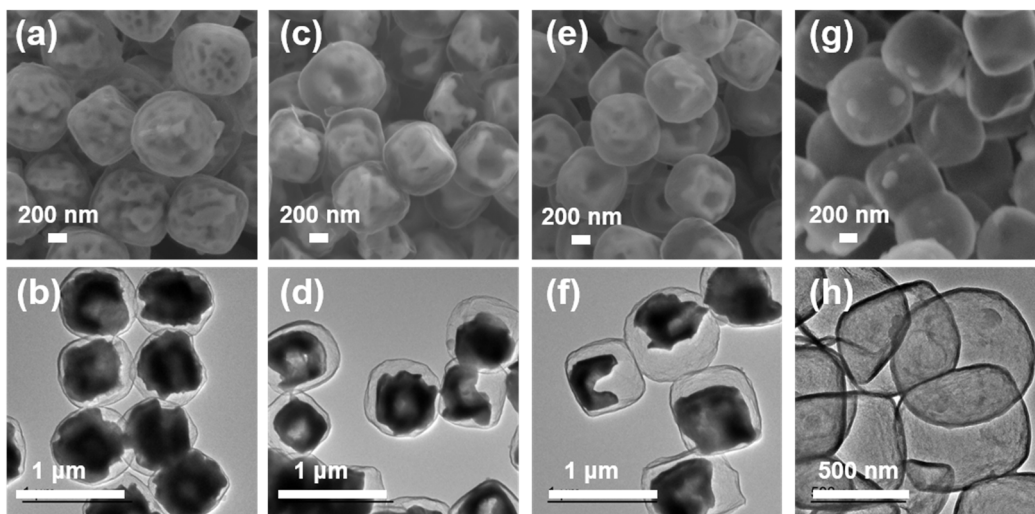


Figure 2. SEM and TEM images of carbonized products after etching for different times: (a,b) $\text{Fe}_3\text{O}_4@void@N$ -doped C-2; (c,d) $\text{Fe}_3\text{O}_4@void@N$ -doped C-5; (e,f) $\text{Fe}_3\text{O}_4@void@N$ -doped C-10; (g,h) the product of 4 mol L^{-1} hydrochloric acid etching for 2 h.

Figure 3 shows the energy dispersive spectroscopy (EDS) element mapping analysis results for the $\text{Fe}_3\text{O}_4@void@N$ -doped C-5 composite. The results show that the $\text{Fe}_3\text{O}_4@void@N$ -doped C-5 composite contains four elements: Fe, O, N, and C. Figure 3d–i show that the carbon layer completely wraps the inner Fe_3O_4 , which is also effective in proving the existence of the core-shell structure. There is an obvious gap between the core and the shell, which is consistent with previous SEM and TEM results. In addition, Figure 3e,f show that N is evenly distributed in the carbon shell, which indicates that nitrogen doping is achieved when PDA is used as a carbon source. In addition, the electron diffraction image (Figure 3c) shows that the Fe_3O_4 core has a single crystal structure.

Figure 4a shows the Raman spectra of the $\text{Fe}_3\text{O}_4@void@N$ -doped C-*x* composite. Raman peaks appear at the positions at about 1300 and 1580 cm^{-1} . The peak around 1300 cm^{-1} is known as the D peak for carbon, which is caused by atomic lattice defects on the surface of the carbon material. The peak at about 1580 cm^{-1} is known as the G peak of carbon, which is formed by the graphitization of carbon material. The appearance of the D peak and the G peak shows that the carbon materials that were formed by dopamine carbonization have internal defects and a certain degree of graphitization. The strength ratio ($I_D:I_G$) of the two peaks of the three composite materials was about 0.65. Because the three composite materials were formed via the etching of $\text{Fe}_3\text{O}_4@N$ -doped C samples at different times, the strengths of peak D and peak G is not affected. In addition, very weak Raman characteristic peaks of Fe_3O_4 also appear at about 200 and 300 cm^{-1} .

Figure 4b–f show the X-ray photoelectron spectroscopy (XPS) analysis results of the $\text{Fe}_3\text{O}_4@void@N$ -doped C-5 composite. The presence of Fe, O, C, and N can be observed from Figure 4b, which proves that the sample is composed of Fe, O, C, and N elements. Two characteristic peaks of Fe 2p can be clearly observed at 711.1 eV and 724.5 eV , respectively (Figure 4c). By calculating the peak area in the spectrogram, it can be known that the ratio of Fe^{3+} to Fe^{2+} is about 2:1, which is in agreement with the ratio of ferric iron to ferrous iron in Fe_3O_4 . For the O 1s spectrogram (Figure 4d), there are three obvious characteristic peaks in the spectrogram at about 530.4 , 532.3 and 533.7 eV , respectively, which correspond to the XPS peak of O^{2-} . For the C 1s spectrogram (Figure 4e), the three smooth peaks at about 284.9 , 286.6 , and 289.1 eV correspond to C–C, C–N and C=O bonds, respectively. The characteristic peaks of graphite nitrogen and pyridine nitrogen can be clearly observed in the N 1s spectrogram (Figure 4f) and correspond to 400.8 eV and 398.5 eV , respectively. Through XPS analysis, it can be further proven that nitrogen-doped carbon is formed after the carbonization of PDA.

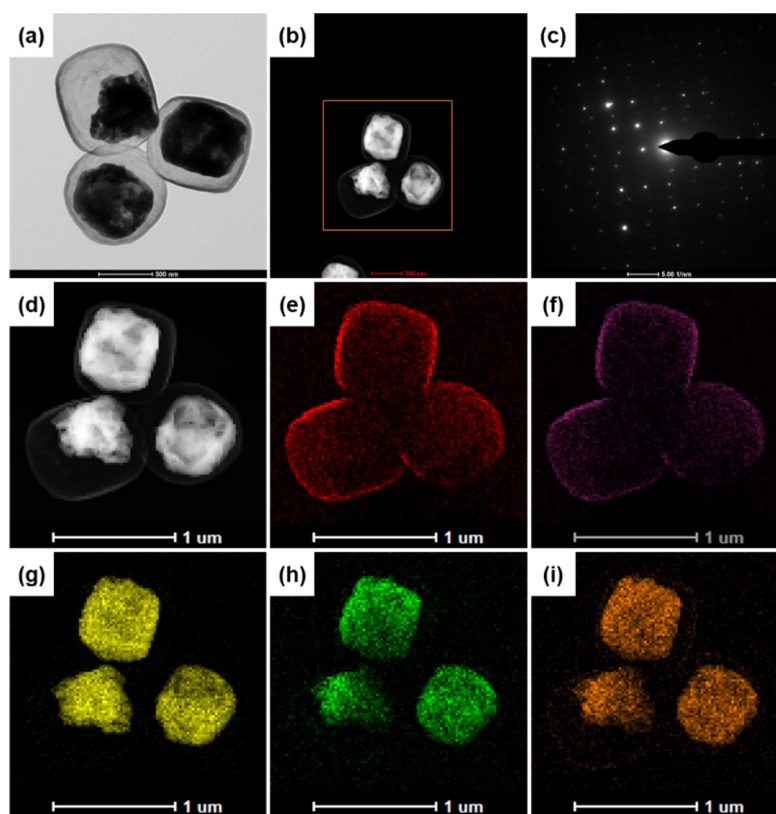


Figure 3. EDS element mapping analysis of $\text{Fe}_3\text{O}_4@void@N$ -doped C-5 composite: (a,b,d) TEM images; (c) electron diffraction photograph; (e) C elements; (f) N elements; (g,h) Fe elements; (i) O elements.

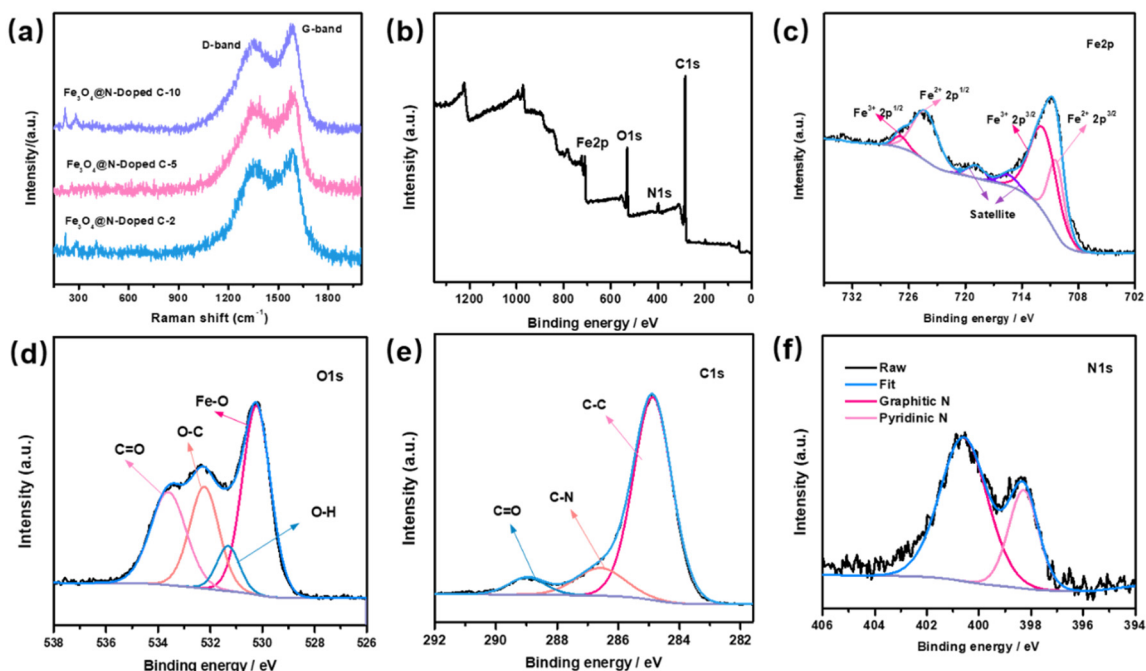


Figure 4. (a) Raman spectra of $\text{Fe}_3\text{O}_4@N$ -doped C- x composites; XPS spectra of $\text{Fe}_3\text{O}_4@void@N$ -doped C-5 composite: (b) full spectrum, (c) Fe 2p, (d) O 1s, (e) C 1s, (f) N 1s.

Figures 5a and S6a, S7a, S8a show the cyclic voltammetry (CV) curves of the Fe_2O_3 and $\text{Fe}_3\text{O}_4@void@N$ -doped C- x composite materials ($x = 2, 5$ and 10) with a voltage range of 0.01 – 3.0 V and a voltage scanning speed of 0.5 mV S^{-1} . In Figure S6a, there is an obvious

reduction peak at 0.43 V in the first cycle of the CV curve. The reduction peak here is due to the reduction of Fe_2O_3 to Fe and the formation of Li_2O ($\text{Fe}_2\text{O}_3 + 6\text{Li}^+ + 6\text{e}^- \rightarrow 2\text{Fe} + 3\text{Li}_2\text{O}$). Due to the solid electrolyte interface (SEI) membrane formed by some of the materials and some of the electrolytes at the same time, the position and intensity of the reduction peak in the following two cycles demonstrate obvious changes [49–51]. In the CV curve, the oxidation peak appears at 1.72 V, where the oxidation process is the oxidation of Fe to Fe^{3+} . In the following two cycles, the oxidation peak appears to have been obviously attenuated, indicating that the cycling performance of the Fe_2O_3 cube sample is poor. Figures 5a and S7a, S8a show the CV curves of the composites of the $\text{Fe}_3\text{O}_4@\text{void@N-doped C-}x$. The main active material in the three composites is Fe_3O_4 , and the reduction reaction that takes place during the first cycling is $\text{Fe}_3\text{O}_4 + 8\text{Li}^+ + 8\text{e}^- \rightarrow 3\text{Fe} + 4\text{Li}_2\text{O}$. The difference between the three samples is only the void size of the core–shell structure. Therefore, their CV curves are basically same. The reduction peak of the $\text{Fe}_3\text{O}_4@\text{void@N-doped C-2}$ in the first cycle is at 0.36 V and tends to be stable after shifting to 0.8 V in the subsequent cycle. The corresponding oxidation peak is at 1.82 V and tends to be stable after shifting to 2 V in the subsequent cycle. In addition, the change trend in the redox peak in the $\text{Fe}_3\text{O}_4@\text{void@N-doped C-5}$ and $\text{Fe}_3\text{O}_4@\text{void@N-doped C-10}$ cycles is similar to that of $\text{Fe}_3\text{O}_4@\text{void@N-doped C-2}$.

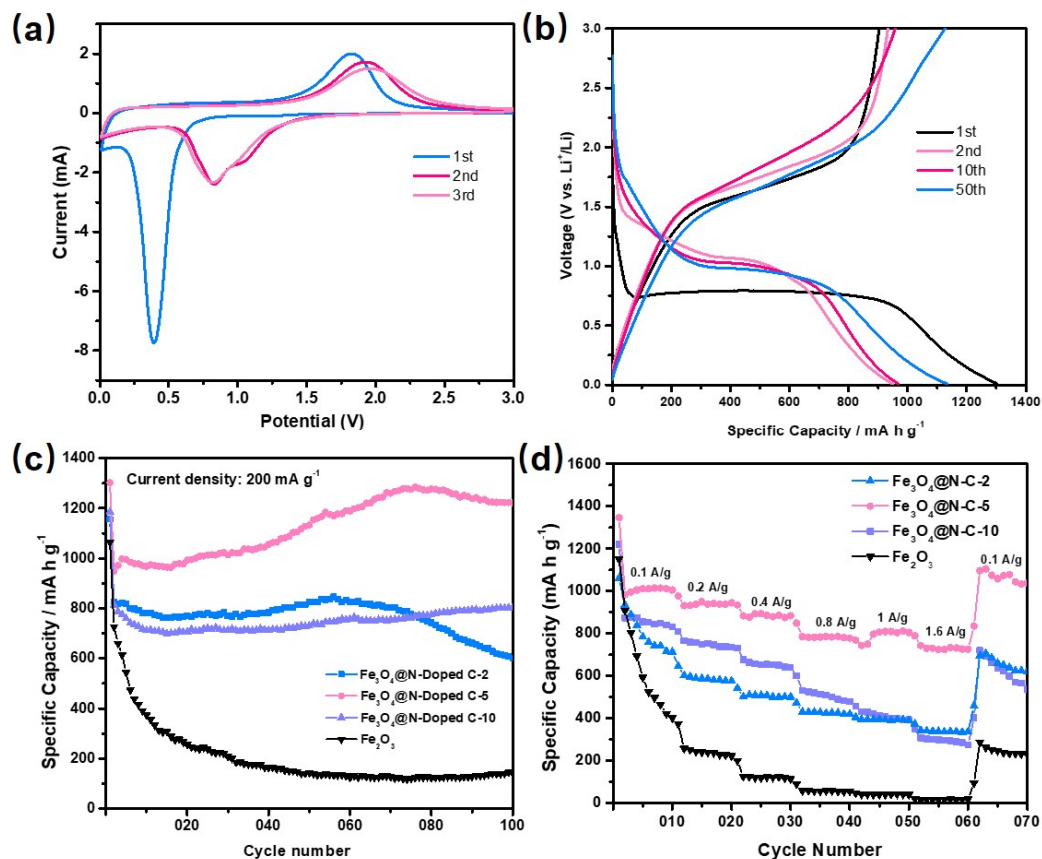


Figure 5. (a) Cyclic voltammetry curve of $\text{Fe}_3\text{O}_4@\text{void@N-doped C-5}$ composite; (b) representative charge–discharge curves of $\text{Fe}_3\text{O}_4@\text{void@N-doped C-5}$ composite; (c) 100 cycle diagrams of Fe_2O_3 and $\text{Fe}_3\text{O}_4@\text{void@N-doped C-}x$ ($x = 2, 5$ and 10) composite at 200 mA g^{-1} current density; (d) rate performance of cubic Fe_2O_3 and $\text{Fe}_3\text{O}_4@\text{void@N-doped C-}x$ composites ($x = 2, 5$ and 10).

Figure S6b shows the charge–discharge curve of the cubic Fe_2O_3 . The current density is 200 mA g^{-1} , and the tested charge–discharge voltage range is 0.01–3 V. It can be observed that the specific capacities of the first discharge and charge cycle of the cubic Fe_2O_3 are $1064.8 \text{ mA h g}^{-1}$ and $690.7 \text{ mA h g}^{-1}$, indicating that the cubic Fe_2O_3 material has a large irreversible capacity for the first cycle. At the 2nd, 10th, and 50th cycles, the discharge

specific capacities are 72.6.4, 373.9, and 143.5 mA h g⁻¹, respectively. The cycle capacity decreases rapidly, indicating that the cycle performance of the cubic Fe₂O₃ is very poor. Figure 5b and Figures S7b, S8b show the representative charge–discharge curves of the first 50 cycles of the Fe₃O₄@void@N-doped C-*x* (*x* = 2, 5, 10) at a 200 mA g⁻¹ current density. It can be observed that the first discharge platform of the three materials is about 0.75 V, which corresponds to the position of a reduction peak in the CV curve. The initial specific discharge capacities of the Fe₃O₄@void@N-doped C-2, Fe₃O₄@void@N-doped C-5, and Fe₃O₄@void@N-doped C-10 are 1155.8, 1302.4, and 1185.9 mA h g⁻¹, respectively. The specific charging capacities are 827.3, 903.6 and 807.8 mA h g⁻¹, respectively, which are lower than the corresponding specific discharge capacities, indicating that the composite also has a specific first irreversible capacity. Relative to the specific initial discharge capacity, the irreversible capacity loss is mainly due to the formation of SEI films. Through the comparison of the four samples, it can be seen that the initial discharge capacity of the composite materials is higher than that of the pure cubic Fe₂O₃, which is due to the nitrogen-doped carbon significantly improving the conductivity of the composite materials. After 50 cycles, the charge–discharge capacity of the cubic Fe₂O₃ is significantly lower than that of the Fe₃O₄@void@N-doped C-*x* composite, and the capacity fading phenomenon is very serious. However, Fe₃O₄@void@N-doped C-*x* still maintains a high specific capacity after 50 cycles, indicating that the cycling performance of the inner Fe₃O₄ core is significantly improved under the protection of the carbon shell. Moreover, after the same 50 cycles, the specific discharge capacities of Fe₂O₃, Fe₃O₄@void@N-doped C-2, Fe₃O₄@void@N-doped C-5, and Fe₃O₄@void@N-doped C-10 are 143.5, 825.8, 1132.9, and 730 mA h g⁻¹, respectively. With the increase in void size, the specific capacity of the composites does not increase correspondingly, and the Fe₃O₄@void@N-doped C-5 material with a suitable core–shell void size shows the maximum specific capacity. The specific capacity of the Fe₃O₄@void@N-doped C-10 is lower than that of Fe₃O₄@void@N-doped C-5. This is probably due to the fact that the relative content of active Fe₃O₄ in Fe₃O₄@void@N-doped C-10 is lower than that of the Fe₃O₄@void@N-doped C-5 sample. For Fe₃O₄@void@C-2, although its Fe₃O₄ content is very high, the high Fe₃O₄ content will result in the composite having low overall conductivity. Therefore, its specific capacity is also lower than that of Fe₃O₄@void@N-doped C-5.

Figure 5c shows the cycle performance diagram of the cube Fe₂O₃ and the Fe₃O₄@void@N-doped C-*x*. The specific discharge capacities of the cubic Fe₂O₃, Fe₃O₄@void@N-doped C-2, Fe₃O₄@void@N-doped C-5, and Fe₃O₄@void@N-doped C-10 are 143.3, 601.4, 1222, and 802.9 mA h g⁻¹ after 100 cycles, respectively, when the current density is 200 mA g⁻¹ and when the charge and discharge voltage range is 0.01–3V. Comparing the four materials, the specific capacity of the carbon-coated composites is significantly higher than that of the simple Fe₂O₃ material. Among them, Fe₃O₄@void@N-doped C-5 has the highest specific capacity, and its capacity continues to increase during the cycle, which is mainly caused by the decomposition of electrolyte. After 60 cycles, the capacity of the Fe₃O₄@void@N-doped C-2 gradually decreases. This is probably due to the small size of the void between the core and shell of the composite material, which cannot completely alleviate the volume deformation of the Fe₃O₄ core during the charging and discharging process. With the increasing number of cycles, the ability of the shell to control the volume deformation of Fe₃O₄ gradually weakens. However, Fe₃O₄@void@N-doped C-5 and Fe₃O₄@void@N-doped C-10 show good cyclic stability due to their large internal void size.

The rate performance of the cubic Fe₂O₃ and Fe₃O₄@void@N-doped C-*x* (*x* = 2, 5 and 10) composites were further tested (Figure 5d). At the current densities of 100, 200, 400, 800, 1000, and 1600 mA g⁻¹, the discharge specific capacities of Fe₃O₄@void@N-doped C-5 were determined to be 1010.2, 955.3, 889.6, 823.6, 833, and 735.5 mA h g⁻¹, respectively. Although the specific capacity of the Fe₃O₄@void@N-doped C-5 composite decreased as the current density increased, it still showed a high specific capacity at 1600 mA g⁻¹, indicating that the composite has a good rate performance. When the current density decreased to 100 mA g⁻¹ again, the specific discharge capacity was able to increase to 1165.8 mA h g⁻¹.

In addition, cyclic tests were also carried out for the Fe_2O_3 and $\text{Fe}_3\text{O}_4@void@N$ -doped C-*x* composites at 800 mA g^{-1} (Figure S10). After 100 cycles, the specific discharge capacities of the cubic Fe_2O_3 , $\text{Fe}_3\text{O}_4@void@N$ -doped C-2, $\text{Fe}_3\text{O}_4@void@N$ -doped C-5, and $\text{Fe}_3\text{O}_4@void@N$ -doped C-10 materials were 67.8, 188, 602.5 and $506.6 \text{ mA h g}^{-1}$, respectively. Compared to the cycle diagram at 200 mA g^{-1} , the cycle performance at the high current density of 800 mA g^{-1} is inferior to that at the low current density of 200 mA g^{-1} . In general, lithium-ion battery electrode materials often show better cycle performance at high current densities. However, for the $\text{Fe}_3\text{O}_4@void@N$ -doped C-*x* composite materials, an abnormal phenomenon occurs. This is probably because the active material in the composite system is a single Fe_3O_4 crystal material with large particles, which is not suitable for charging and discharging with large currents. The electrochemical performance of the $\text{Fe}_3\text{O}_4@void@N$ -doped C-5 was compared to the results from reports that have previously been published in the literature. The specific capacity and cycling performance of the $\text{Fe}_3\text{O}_4@void@N$ -doped C-5 at 200 mA g^{-1} reached the level of other similar Fe_3O_4 -based anode materials [52,53].

By comparing the related electrochemical test data above, among all of the composites, the $\text{Fe}_3\text{O}_4@void@N$ -doped C-5 composite has the best cycling performance and rate performance. This is directly related to the appropriate acid etching time. The proper pore size between the carbon shell and the Fe_3O_4 core in the $\text{Fe}_3\text{O}_4@void@N$ -doped C-5 material (larger than $\text{Fe}_3\text{O}_4@void@N$ -doped C-2) can effectively alleviate the volume expansion of Fe_3O_4 during the cycle and can also facilitate electrolyte diffusion and the transmission of lithium ions. In addition, the relatively high content of the Fe_3O_4 active substance in the material (more than in $\text{Fe}_3\text{O}_4@void@N$ -doped C-10) ensures its large specific capacity. After 100 cycles, the electrode based on $\text{Fe}_3\text{O}_4@void@N$ -doped C-5 was characterized via SEM and TEM (Figures S11 and S12). The results show that the structure is essentially retained after 100 cycles. This indicates the good structural stability of the material during the charge/discharge process.

The electrochemical impedance spectroscopy (EIS) of the assembled lithium-ion battery was also measured in more detail. As shown in Figure S13, the EIS curves of the cube Fe_2O_3 and the $\text{Fe}_3\text{O}_4@void@N$ -doped C-*x* composite are composed of a small semicircle and a straight line. The small semicircle in the high frequency region is related to the charge transmission process of the electrons and lithium ions at the conductive junction. The lines in the low-frequency region are related to the solid diffusion process of the lithium ions in the active material. It can be observed that the diameter of the small semicircular cube Fe_2O_3 is larger than that of the $\text{Fe}_3\text{O}_4@void@N$ -doped C-*x* composite, indicating that its electrical conductivity is worse than that of the $\text{Fe}_3\text{O}_4@void@N$ -doped C-*x* composite. The good conductivity of the composites can be attributed to the carbon coating formed by dopamine, which contains many unsaturated bonds (such as C=N and C=C bonds) that are able to provide a large number of excellent conductive matrices for Fe_3O_4 . In addition, the lines in the low-frequency region are all close to 45° , indicating that the lithium ions have good diffusion ability in the active materials.

3. Conclusions

In this work, PDA was used as a carbon source to coat Fe_2O_3 cubes to form a nitrogen-doped carbon coating layer. Further, the acid etching method was used to prepare composite materials with a core-shell structure and with different void sizes to act as the electrode materials in a lithium-ion battery. The electrochemical test results show that the specific capacity of the composites did not increase as the void size increased. Among all of the samples, the $\text{Fe}_3\text{O}_4@void@N$ -doped C-5 with the appropriate void size showed the largest specific capacity, the best cycling performance, and the best rate performance. At a current density of 200 mA g^{-1} , the discharge capacity of the $\text{Fe}_3\text{O}_4@void@N$ -doped C-5 was able to reach 1222 mA h g^{-1} after 100 cycles, which is much higher than the levels achieved by the cubic Fe_2O_3 . The appropriate size of the void between the carbon shell and the Fe_3O_4 core is not only beneficial to alleviate the volume expansion of Fe_3O_4 during the cycle, but also to electrolyte diffusion and the transmission of lithium ions.

Supplementary Materials: The following supporting information can be downloaded via the following, Figure S1. (a) XRD patterns of cubic Fe_2O_3 and standard card; (b) XRD patterns of $\text{Fe}_3\text{O}_4@void@N$ -Doped C-2 composite and standard card; Figure S2. (a,b) SEM images of cubic Fe_2O_3 at different magnification; Figure S3. (a,b) SEM images of cubic $\text{Fe}_2\text{O}_3@PDA$ at different magnification; Figure S4. (a,b) SEM images of cubic $\text{Fe}_3\text{O}_4@N$ -Doped C at different magnification; Figure S5. The thermogravimetric analysis curves of $\text{Fe}_3\text{O}_4@void@N$ -doped C- x composite ($x = 2, 5$ and 10); Figure S6. (a) Cyclic voltammetry curves of the first three cycles of cubic Fe_2O_3 ; (b) Representative charge-discharge curves of cubic Fe_2O_3 ; Figure S7. (a) Cyclic voltammetry curves of $\text{Fe}_3\text{O}_4@void@N$ -Doped C-2 composite; (b) Representative charge-discharge curves of $\text{Fe}_3\text{O}_4@void@N$ -Doped C-2 composite; Figure S8. (a) Cyclic voltammetry curves of $\text{Fe}_3\text{O}_4@void@N$ -Doped C-10 composites; (b) Representative charge-discharge curves of $\text{Fe}_3\text{O}_4@void@N$ -Doped C-10 composites; Figure S9. dQ/dV curves of all samples for C/D profiles during the second cycling; Figure S10. 100 cycle diagrams of cubic Fe_2O_3 and $\text{Fe}_3\text{O}_4@void@N$ -Doped C- x ($x = 2, 5$ and 10) composites at 800 mA g^{-1} current density; Figure S11. SEM images of $\text{Fe}_3\text{O}_4@void@N$ -doped C after 100 cycles; Figure S12. TEM images of $\text{Fe}_3\text{O}_4@void@N$ -doped C after 100 cycles; Figure S13. EIS curves of cubic Fe_2O_3 and $\text{Fe}_3\text{O}_4@void@N$ -Doped C- x composites; Figure S14. Field-dependent magnetization curve of Fe_2O_3 measured at room temperature

Author Contributions: Data curation, J.W., Q.H., W.H.; writing—original draft preparation, J.W., Q.H., W.Z., Y.W.; writing—review and editing, K.P., M.Z., H.P.; funding acquisition, K.P., M.Z., H.P. All authors have read and agreed to the published version of the manuscript.

Funding: This research was supported by the National Natural Science Foundation of China (NSFC-U1904215), the Fundamental Research Funds for the Central Universities (No. NS2021039), the Top-notch Academic Programs Project of Jiangsu Higher Education Institutions (TAPP), the Natural Science Foundation of Jiangsu Province (BK20200044), the Program for Young Changjiang Scholars of the Ministry of Education (Q2018270), And the Open Fund of the National Joint Engineering Research Center for abrasion control and molding of metal materials (HKDNM2019010). We also acknowledge the Priority Academic Program Development of Jiangsu Higher Education Institutions and the technical support we received at the Testing Center of Yangzhou University.

Institutional Review Board Statement: Not applicable.

Informed Consent Statement: Not applicable.

Data Availability Statement: Not applicable.

Conflicts of Interest: The authors declare no conflict of interest.

Sample Availability: Samples of the compounds are not available from the authors.

References

1. Kim, H.; Hong, J.; Park, K.-Y.; Kim, H.; Kim, S.-W.; Kang, K. 3D-0D Graphene- Fe_3O_4 Quantum Dot Hybrids as High-Performance Anode Materials for Sodium-Ion Batteries. *Chem. Rev.* **2014**, *114*, 11788–11827. [[CrossRef](#)]
2. Yuan, C.; Wu, H.B.; Xie, Y.; Lou, X.W. Mixed Transition-Metal Oxides: Design, Synthesis, and Energy-Related Applications. *Angew. Chem. Int. Ed.* **2014**, *53*, 1488–1504. [[CrossRef](#)]
3. Hu, W.; Zheng, M.; Xu, B.; Wei, Y.; Zhu, W.; Li, Q.; Pang, H. Design of Hollow Carbon-based Materials Derived from Metal–Organic Frameworks for Electrocatalysis and Electrochemical Energy Storage. *J. Mater. Chem. A* **2021**, *9*, 3880–3917. [[CrossRef](#)]
4. Du, M.; Li, Q.; Zhao, Y.; Liu, C.S.; Pang, H. A Review of Electrochemical Energy Storage Behaviors Based on Pristine Metal–Organic Frameworks and Their Composites. *Coord. Chem. Rev.* **2020**, *416*, 213341. [[CrossRef](#)]
5. Singh, G.K. Solar Power Generation by PV (Photovoltaic) Technology: A Review. *Energy* **2013**, *53*, 1–13. [[CrossRef](#)]
6. Chen, B.; Yang, Y.; Wang, Z.L. Scavenging Wind Energy by Triboelectric Nanogenerators. *Adv. Energy Mater.* **2018**, *8*, 1702649. [[CrossRef](#)]
7. Rourke, F.O.; Boyle, F.; Reynolds, A. Tidal Energy Update 2009. *Appl. Energy* **2010**, *87*, 398–409. [[CrossRef](#)]
8. Liu, H.; Jia, M.; Zhu, Q.; Cao, B.; Chen, R.; Wang, Y.; Wu, F.; Xu, B. 3D-0D Graphene- Fe_3O_4 Quantum Dot Hybrids as High-Performance Anode Materials for Sodium-Ion Batteries. *ACS Appl. Mater. Interfaces* **2016**, *8*, 26878–26885. [[CrossRef](#)]
9. Guo, M.; Balamurugan, J.; Li, X.; Kim, N.H.; Lee, J.H. Hierarchical 3D Cobalt-Doped Fe_3O_4 Nanospheres@NG Hybrid as an Advanced Anode Material for High-Performance Asymmetric Supercapacitors. *Small* **2017**, *13*, 1701275. [[CrossRef](#)]
10. Cao, X.; Tan, C.; Zhang, X.; Zhao, W.; Zhang, H. Solution-Processed Two-Dimensional Metal Dichalcogenide-Based Nanomaterials for Energy Storage and Conversion. *Adv. Mater.* **2016**, *28*, 6167–6196. [[CrossRef](#)]

11. Lv, T.-T.; Liu, Y.-Y.; Wang, H.; Yang, S.-Y.; Liu, C.-S.; Pang, H. Crystal Water Enlarging The Interlayer Spacing of Ultrathin $V_2O_5 \cdot 4VO_2 \cdot 2.72H_2O$ Nanobelts for High-Performance Aqueous Zinc-Ion Battery. *Chem. Eng. J.* **2021**, *411*, 128533. [[CrossRef](#)]
12. Shan, Y.; Zhang, M.Y.; Bai, Y.; Du, M.; Guo, X.; Pang, H. Design and Synthesis of Transition Metal Oxide/Zeolitic Imidazolate Framework-67 Composites. *Chem. Eng. J.* **2022**, *429*, 132146. [[CrossRef](#)]
13. Tang, W.; Zhu, Y.; Hou, Y.; Liu, L.; Wu, Y.; Loh, K.P.; Zhang, H.; Zhu, K. Aqueous Rechargeable Lithium Batteries as An Energy Storage System of Superfast Charging. *Energy Environ. Sci.* **2013**, *6*, 2093–2104. [[CrossRef](#)]
14. Goodenough, J.B.; Park, K.-S. The Li-Ion Rechargeable Battery: A Perspective. *J. Am. Chem. Soc.* **2013**, *135*, 1167–1176. [[CrossRef](#)] [[PubMed](#)]
15. Croguennec, L.; Palacin, M.R. Recent Achievements on Inorganic Electrode Materials for Lithium-Ion Batteries. *J. Am. Chem. Soc.* **2015**, *137*, 3140–3156. [[CrossRef](#)]
16. Li, F.-S.; Wu, Y.-S.; Chou, J.; Winter, M.; Wu, N.-L. A Mechanically Robust and Highly Ion-Conductive Polymer-Blend Coating for High-Power and Long-Life Lithium-Ion Battery Anodes. *Adv. Mater.* **2015**, *27*, 130–137. [[CrossRef](#)] [[PubMed](#)]
17. Li, M.; Lu, J.; Chen, Z.; Amine, K. 30 Years of Lithium-Ion Batteries. *Adv. Mater.* **2018**, *30*, 1800561. [[CrossRef](#)] [[PubMed](#)]
18. Qin, J.; He, C.; Zhao, N.; Wang, Z.; Shi, C.; Liu, E.-Z.; Li, J. Graphene Networks Anchored with Sn@Graphene as Lithium Ion Battery Anode. *ACS Nano* **2014**, *8*, 1728–1738. [[CrossRef](#)]
19. Liu, Y.; Zhang, N.; Jiao, L.; Tao, Z.; Chen, J. Ultrasmall Sn Nanoparticles Embedded in Carbon as High-Performance Anode for Sodium-Ion Batteries. *Adv. Funct. Mater.* **2015**, *25*, 214–220. [[CrossRef](#)]
20. Wu, S.; Han, C.; Iocozzia, J.; Lu, M.; Ge, R.; Xu, R.; Lin, Z. Germanium-Based Nanomaterials for Rechargeable Batteries. *Angew. Chem. Int. Ed.* **2016**, *55*, 7898–7922. [[CrossRef](#)]
21. Kwon, H.-T.; Lee, C.K.; Jeon, K.-J.; Park, C.-M. Silicon Diphosphide: A Si-Based Three-Dimensional Crystalline Framework as a High-Performance Li-Ion Battery Anode. *ACS Nano* **2016**, *10*, 5701–5709. [[CrossRef](#)] [[PubMed](#)]
22. Liu, X.; Huang, J.-Q.; Zhang, Q.; Mai, L. Nanostructured Metal Oxides and Sulfides for Lithium–Sulfur Batteries. *Adv. Mater.* **2017**, *29*, 1601759. [[CrossRef](#)]
23. Xu, X.; Shen, J.; Li, F.; Wang, Z.; Zhang, D.; Zuo, S.; Liu, J. $Fe_3O_4@C$ Nanotubes Grown on Carbon Fabric as a Free-Standing Anode for High-Performance Li-Ion Batteries. *Chem. A Eur. J.* **2020**, *26*, 14708–14717. [[CrossRef](#)]
24. Liu, J.; Xu, X.; Hu, R.; Yang, L.; Zhu, M. Uniform Hierarchical $Fe_3O_4@Polypyrrole$ Nanocages for Superior Lithium Ion Battery Anodes. *Adv. Energy Mater.* **2016**, *6*, 1600256. [[CrossRef](#)]
25. Huang, Y.; Li, Y.; Huang, R.; Yao, J. Ternary $Fe_2O_3/Fe_3O_4/FeCO_3$ Composite as a High-Performance Anode Material for Lithium-Ion Batteries. *J. Phys. Chem. C* **2019**, *123*, 12614–12622. [[CrossRef](#)]
26. Zheng, M.; Tang, H.; Li, L.; Hu, Q.; Zhang, L.; Xue, H.; Pang, H. Hierarchically Nanostructured Transition Metal Oxides for Lithium-Ion Batteries. *Adv. Sci.* **2018**, *5*, 1700592. [[CrossRef](#)]
27. Yu, S.-H.; Lee, S.H.; Lee, D.J.; Sung, Y.-E.; Hyeon, T. Conversion Reaction-Based Oxide Nanomaterials for Lithium Ion Battery Anodes. *Small* **2016**, *12*, 2146–2172. [[CrossRef](#)]
28. Li, Q.; Li, H.; Xia, Q.; Hu, Z.; Zhu, Y.; Yan, S.; Ge, C.; Zhang, Q.; Wang, X.; Shang, X.; et al. Extra Storage Capacity in Transition Metal Oxide Lithium-Ion Batteries Revealed by in Situ Magnetometry. *Nat. Mater.* **2021**, *20*, 76–83.
29. Fang, S.; Bresser, D.; Passerini, S. Transition Metal Oxide Anodes for Electrochemical Energy Storage in Lithium- and Sodium-Ion Batteries. *Adv. Energy Mater.* **2020**, *10*, 1902485. [[CrossRef](#)]
30. Cho, J.S.; Hong, Y.J.; Kang, Y.C. Design and Synthesis of Bubble-Nanorod-Structured Fe_2O_3 –Carbon Nanofibers as Advanced Anode Material for Li-Ion Batteries. *ACS Nano* **2015**, *9*, 4026–4035. [[CrossRef](#)]
31. Zeng, Y.; Yu, M.; Meng, Y.; Fang, P.; Lu, X.; Tong, Y. Iron-Based Supercapacitor Electrodes: Advances and Challenges. *Adv. Energy Mater.* **2016**, *6*, 1601053. [[CrossRef](#)]
32. Ma, J.; Guo, X.; Yan, Y.; Xue, H.; Pang, H. FeOx-Based Materials for Electrochemical Energy Storage. *Adv. Sci.* **2018**, *5*, 1700986. [[CrossRef](#)]
33. Wan, Y.; Yang, Z.; Xiong, G.; Guo, R.; Liu, Z.; Luo, H. Anchoring Fe_3O_4 Nanoparticles on Three-Dimensional Carbon Nanofibers toward Flexible High-Performance Anodes for Lithium-Ion Batteries. *J. Power Sources* **2015**, *294*, 414–419. [[CrossRef](#)]
34. Wang, J.; Gao, M.; Pan, H.; Liu, Y.; Zhang, Z.; Li, J.; Su, Q.; Du, G.; Zhu, M.; Ouyang, L.; et al. Mesoporous Fe_2O_3 Flakes of High Aspect Ratio Encased within Thin Carbon Skeleton for Superior Lithium-Ion Battery Anodes. *J. Mater. Chem. A* **2015**, *3*, 14178–14187. [[CrossRef](#)]
35. Fu, C.; Mahadevegowda, A.; Grant, P.S. Fe_3O_4 /Carbon Nanofibres with Necklace Architecture for Enhanced Electrochemical Energy Storage. *J. Mater. Chem. A* **2015**, *3*, 14245–14253. [[CrossRef](#)]
36. Li, X.; Ma, Y.; Cao, G.; Qu, Y. FeOx@Carbon Yolk/Shell Nanowires with Tailored Void Spaces as Stable and High-Capacity Anodes for Lithium Ion Batteries. *J. Mater. Chem. A* **2016**, *4*, 12487–12496. [[CrossRef](#)]
37. Xu, Z.L.; Yao, S.; Cui, J.; Zhou, L.; Kim, J.K. Atomic Scale, Amorphous FeOx/Carbon Nanofiber Anodes for Li-Ion and Na-Ion Batteries. *Energy Storage Mater.* **2017**, *8*, 10–19. [[CrossRef](#)]
38. Zhao, Y.; Li, X.; Yan, B.; Xiong, D.; Li, D.; Lawes, S.; Sun, X. Recent Developments and Understanding of Novel Mixed Transition-Metal Oxides as Anodes in Lithium Ion Batteries. *Adv. Energy Mater.* **2016**, *6*, 1502175. [[CrossRef](#)]
39. Li, X.; Zhang, Z.; Li, J.; Ma, Y.; Qu, Y. Structural Influence of Porous FeOx@C Nanorods on Their Performance as Anodes of Lithium-Ion Batteries. *J. Mater. Chem. A* **2015**, *3*, 18649–18656. [[CrossRef](#)]

40. Zhang, H.; Zhou, L.; Noonan, O.; Martin, D.J.; Whittaker, A.K.; Yu, C. Tailoring the Void Size of Iron Oxide@Carbon Yolk–Shell Structure for Optimized Lithium Storage. *Adv. Funct. Mater.* **2014**, *24*, 4337–4342. [[CrossRef](#)]
41. Wu, Q.; Zhao, R.; Liu, W.; Zhang, X.; Shen, X.; Li, W.; Diao, G.; Chen, M. In-Depth Nanocrystallization Enhanced Li-Ions Batteries Performance with Nitrogen-Doped Carbon Coated Fe₃O₄ Yolk–Shell Nanocapsules. *J. Power Sources* **2017**, *344*, 74–84. [[CrossRef](#)]
42. Kim, J.H.; Kang, Y.C. Synthesis of Uniquely Structured Yolk–Shell Metal Oxide Microspheres Filled with Nitrogen-Doped Graphitic Carbon with Excellent Li–Ion Storage Performance. *Small* **2017**, *13*, 1701585. [[CrossRef](#)] [[PubMed](#)]
43. Wang, L.; Yang, C.; Dou, S.; Wang, S.; Zhang, J.; Gao, X.; Ma, J.; Yu, Y. Nitrogen-Doped Hierarchically Porous Carbon Networks: Synthesis and Applications in Lithium-Ion Battery, Sodium-Ion Battery and Zinc-Air Battery. *Electrochim. Acta* **2016**, *219*, 592–603. [[CrossRef](#)]
44. Yang, L.; Guo, G.; Sun, H.; Shen, X.; Hu, J.; Dong, A.; Yang, D. Ionic Liquid as the C and N Sources to Prepare Yolk-shell Fe₃O₄@N-doped Carbon Nanoparticles and its High Performance in Lithium-ion Battery. *Electrochim. Acta* **2016**, *190*, 797–803. [[CrossRef](#)]
45. Sun, M.; Zhang, G.; Liu, H.; Liu, Y.; Li, J. α - and γ -Fe₂O₃ Nanoparticle/Nitrogen Doped Carbon Nanotube Catalysts for High-Performance Oxygen Reduction Reaction. *Sci. China Mater.* **2015**, *58*, 683–692. [[CrossRef](#)]
46. Lei, C.; Han, F.; Li, D.; Li, W.-C.; Sun, Q.; Zhang, X.-Q.; Lu, A.-H. Dopamine as The Coating Agent and Carbon Precursor for The Fabrication of N-Doped Carbon Coated Fe₃O₄ Composites as Superior Lithium Ion Anodes. *Nanoscale* **2013**, *5*, 1168–1175. [[CrossRef](#)]
47. Wang, H.; Zheng, Y.; Peng, Z.; Liu, X.; Qu, C.; Huang, Z.; Cai, Z.; Fan, H.; Zhang, Y. Nanocavity-Enriched Co₃O₄@ZnCo₂O₄@NC Porous Nanowires Derived from 1D Metal Coordination Polymers for Fast Li⁺ Diffusion Kinetics and Super Li⁺ Storage. *Dalt. Trans.* **2021**, *50*, 7277–7283. [[CrossRef](#)] [[PubMed](#)]
48. Chen, Y.; Shi, L.; Li, D.; Dong, Y.; Yuan, Q.; Huang, S.; Yang, H.Y.; Wei, X.; Zhuang, Q.; Ju, Z.; et al. Undercooling-Directed NaCl Crystallization: An Approach towards Nanocavity-Linked Graphene Networks for Fast Lithium and Sodium Storage. *Nanoscale* **2020**, *12*, 7622–7630. [[CrossRef](#)]
49. Luo, Y.; Luo, J.; Jiang, J.; Zhou, W.; Yang, H.; Qi, X.; Zhang, H.; Fan, H.J.; Yu, D.Y.W.; Li, C.M.; et al. Seed-Assisted Synthesis of Highly Ordered TiO₂@ α -Fe₂O₃ Core/Shell Arrays on Carbon Textiles for Lithium-Ion Battery Applications. *Energy Environ. Sci.* **2012**, *5*, 6559–6566. [[CrossRef](#)]
50. Zheng, F.; He, M.; Yang, Y.; Chen, Q. Nano Electrochemical Reactors of Fe₂O₃ Nanoparticles Embedded in Shells of Nitrogen-Doped Hollow Carbon Spheres as High-Performance Anodes for Lithium-Ion Batteries. *Nanoscale* **2015**, *7*, 3410–3417. [[CrossRef](#)] [[PubMed](#)]
51. Yin, L.; Gao, Y.J.; Jeon, I.; Yang, H.; Kim, J.P.; Jeong, S.Y.; Cho, C.R. Rice-Panicle-Like γ -Fe₂O₃@C Nanofibers as High-Rate Anodes for Superior Lithium-Ion Batteries. *Chem. Eng. J.* **2019**, *356*, 60–68. [[CrossRef](#)]
52. Na, Z.; Yao, R.; Yan, Q.; Wang, X.; Sun, X.; Wang, X. A General Strategy for Enabling Fe₃O₄ with Enhanced Lithium Storage Performance: Synergy between Yolk-Shell Nanostructures and Doping-Free Carbon. *Electrochim. Acta* **2021**, *367*, 137464. [[CrossRef](#)]
53. Zhang, J.; Wang, K.; Xu, Q.; Zhou, Y.; Cheng, F.; Guo, S. Beyond Yolk–Shell Nanoparticles: Fe₃O₄@Fe₃C Core@Shell Nanoparticles as Yolks and Carbon Nanospindles as Shells for Efficient Lithium Ion Storage. *ACS Nano* **2015**, *9*, 3369–3376. [[CrossRef](#)] [[PubMed](#)]